Insect Flight Muscles: Inspirations for Motion Control in Flapping-Wing MAVs

Hosein Mahjoubi, and Katie Byl

Abstract—**Micro-aerial vehicles (MAV) and their promising applications – such as undetected surveillance or exploration of environments with little space for land-based maneuvers – are a well-known topic in the field of aerial robotics. Inspired by high maneuverability and agile flight of insects, over the past two decades a significant amount of effort has been dedicated to research on flapping-wing MAVs, most of which aim to address unique challenges in morphological construction, force production, and control strategy. Although remarkable solutions have been found for sufficient lift generation, effective methods for motion control still remain an open problem. The focus of this paper is to investigate general flight control mechanisms that are potentially used by real insects, thereby providing inspirations for flapping-wing MAV control. Through modeling the insect flight muscles, we show that stiffness and set point of the wing's joint can be respectively tuned to regulate the wing's lift and thrust forces. Therefore, employing a suitable controller with variable impedance actuators at each wing joint is a prospective approach to agile flight control of insect-inspired MAVs. The results of simulated flight experiments with one such controller are provided and support our claim.**

Keywords—*Aerial Robotics; Microrobotics; Insect Flight; Muscle Model; Wing Rotation; Tunable Impedance; Variable Stiffness Actuator; Insect-inspired MAVs; Maneuverability.*

I. INTRODUCTION

THE agility of insects and hummingbirds in flight provides inspiration for the design and control of small micro-aerial vehicles (MAVs). Identifying and exploiting basic principles that can be used in man-made MAV designs has been, correspondingly, an active area of research in recent years. Many high-level questions remain in designing small, flapping-wing devices to exploit low Reynolds flapping-wing aerodynamics. For example, it is of interest to know the extent to which achieving both stable flight and agile maneuvering relies on 1) active control of wing shape and/or orientation during flapping, 2) high-bandwidth actuation and control loops, and 3) accurate sensing of full state information. Toward addressing such questions, we suggest first exploring the theoretical limits of insect muscle, from a control theory perspective.

Specifically, given the current biological understanding of the capabilities and limitations of insect muscle, we wish

H. Mahjoubi and K. Byl are with the Robotics Laboratory, Department of Electrical and Computer Engineering, University of California at Santa Barbara, Santa Barbara, CA 93106 USA (e-mail: h.mahjoubi@ece.ucsb.edu, katiebyl@ece.ucsb.edu).

to formulate likely hypotheses on the underlying control principles employed by insects. Such principles would then provide starting points for design and control of agile, insect-scale robots.

In this paper, we investigate a potential strategy that might be used by insects for controlling aerodynamic forces. Inspired by the structure and function of insect muscles, this strategy relies on a tunable mechanical structure that employs quadratic springs. Although it remains an open question whether this approach is in fact employed by insects, we show that it is theoretically capable of controlling lift and thrust forces in flapping-wing MAVs. Furthermore, this approach allows us to decouple the lift and thrust forces on a wing to a considerable extent. Thus, simple controllers such as PIDs could be used to control the vehicle. One such controller is used to simulate the flight of a dragonfly/hummingbird-scale MAV. The results suggest that this control approach can handle various agile maneuvers while maintaining its stability.

The remainder of the paper is organized as follows. Section II reviews the types and functionality of flight muscles in insects. Using simple muscle models, a mechanical model of the wing joint is then developed. Section III presents a simple quasi-steady-state model of the aerodynamics involved in insect flight. In Section IV, we use these models to explain how rotation of the wing is governed by the interaction between aerodynamic force and impedance properties of the wing joint. There, we will show how adjusting these impedance properties can be used to regulate lift and thrust forces. The dynamic model of the MAV and the designed controller are discussed in sections V and VI, respectively. The results of simulated flight control experiments will be presented in section VII. Finally, section VIII concludes this work.

II. FLIGHT MUSCLES IN INSECTS

Many flying insects employ two types of muscles during flight: *synchronous* and *asynchronous* [1]. Here, we will first briefly review the physical structure and functionality of each group. Those muscles that have the main role in adjustment of aerodynamic forces and maneuverability are then used as a template to develop a mechanical model of wing actuation.

A. Structure and Functionality

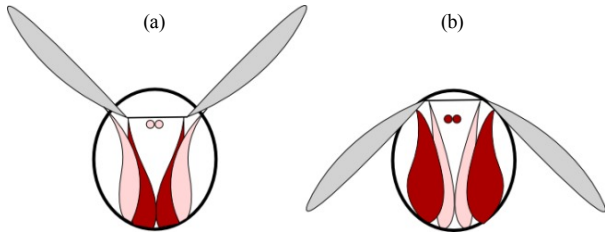More ancient aerobaticists of the insect world such as

Fig. 1. An illustration of insect's wing stroke using synchronous muscles: (a) upstroke and (b) downstroke. Muscles in the process of contraction are shown in a darker color (adapted from [2]).

Fig. 3. (a) Wing cross-section (during downstroke) at its center of pressure, illustrating the pitch angle of the wing ψ, and its angle of attack α_r with respect to the air flow u_r. Normal and tangential aerodynamic forces are shown by F_N and F_{Tn}. F_L and F_T represent the lift and thrust components of the overall force. (b) Overhead view of the wing/body setup which defines the stroke angle ϕ.

dragonflies use only synchronous muscles, which power the wings directly as illustrated in Fig. 1. Contraction of the muscles attached to the base of the wing inside the pivot point raises the wing (Fig. 1.a) while it is brought down by a contraction of muscles that attach to the wing outside of the pivot point (Fig. 1.b) [1]-[2].

As the naming suggests, synchronous muscles contract once for every nerve impulse [1] which is why purely synchronous muscled insects fly at lower flapping frequencies. Therefore, to produce sufficient lift force, these insects often have large wings [3]. For example, a locust that beats its wings at 16 Hz has a wing area of 6-7 cm² [4].

Asynchronous muscles are found in more advanced insects such as true flies. In evolutionary terms, these muscles are a new design feature which has facilitated the evolution of smaller and much faster agile flyers.

Asynchronous muscles are primarily responsible for power generation. As shown in Fig. 2, they indirectly move the wings by exciting a resonant mechanical load in the body structure [1]. When operating against inertial load of the air moved by the wings, these muscles act as a self-sustaining oscillator that may execute several stroke cycles for every electrical stimulus received [5]. This justifies how some insects can achieve very high flapping frequencies, e.g. 1000 Hz for a small midge [4].

From Fig. 2, it can be observed that contraction of each pair of asynchronous muscles indirectly operates both wings and thus, may adjust the stroke magnitude and frequency of flapping. Both of these parameters influence the velocity of air currents across the wings. From basic aerodynamic theory, we know that the relative velocity of air flow directly affects the magnitude of overall aerodynamic force. Hence, we can see that asynchronous muscles play a major role in production and adjustment of this force. However, lift and
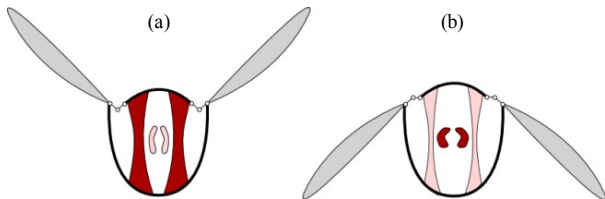

Fig. 2. An illustration of insect's wing stroke using asynchronous muscles: (a) upstroke and (b) downstroke. Muscles in the process of contraction are shown in a darker color (adapted from [2]).
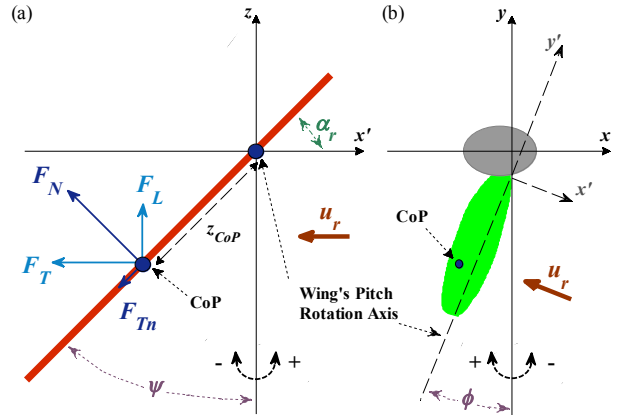
thrust components of the overall force produced by each wing depend on the angle of attack (AoA) of that wing (Fig. 3.a). Being indirectly connected to the wings (Fig. 2), asynchronous muscles are primarily used to power the wings rather than regulating their angles of attack. Therefore, contribution of these muscles to individual control of lift and thrust forces should be negligible.

The structure of synchronous muscles, by contrast, allows them to directly influence both the wing stroke motion and its pitch rotation (Fig. 1). Thus, these muscles can manipulate the angle of attack of each wing separately in order to adjust the lift and thrust components of its aerodynamic force, and thereby generate thrust or steering forces.

From this review, one can see that flight control is primarily the role of synchronous muscles. Next, we develop a simple mechanical model based on the interaction between these muscles and the wings. This model will be then used to help us better understand the control process of aerodynamic force.

B. Mechanical Model

To adopt the proper angle of attack during each half stroke, the wing has to supinate before the upstroke and pronate before the downstroke [1]. This means that pitch rotation of the wing is a cyclic motion which happens at a rate close to that of the flapping frequency. However, this frequency is usually a lot larger than the stimulation rate – bandwidth limitation – of synchronous muscles [1], [5]. Therefore, these muscles cannot be directly responsible for the fast rotational motion of the wings. In fact, this motion is powered by the torque due to aerodynamic force F_N with respect to the wing's pitch rotation axis (Fig. 3.a).

Like most muscle-joint structures, contraction of agonist/antagonist synchronous muscles can change the stiffness of the joint [1], [5]. This stiffness results in a
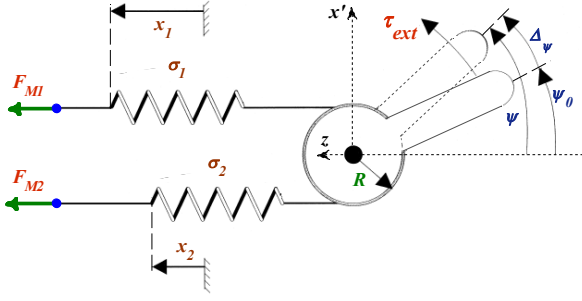
Fig. 4. A simplified mechanical model of synchronous muscle-joint structure. Each muscle is modeled as a nonlinear spring with variable stiffness σ_i ($i=1,2$). A force of F_{Mi} pulls the input side of each spring, resulting in the displacement x_i. The other sides of both springs are attached to a pulley of radius R which represents the wing's joint.

resistive torque that opposes the rotation of the wing. With a stiffer joint, the rotation range of the wing will be more limited. Thus, synchronous muscles can influence the angle of attack through adjusting the stiffness of the joint. These muscles can also slowly rotate the wings and by doing so, bias the angle of attack. This would result in a phase shift between wing stroke and wing rotation which is often observed during steering or thrust [6].

A simplified model for muscle consists of a force pulling one end of a nonlinear spring [7]. The other end is attached to the joint. Here, we model the joint as a pulley of radius R, whose axis of rotation is the same as wing's pitch rotation axis. Fig. 4 illustrates the complete diagram of the model for one wing and the pair of synchronous muscles attached to it.

The forces that model the power of muscle contraction are represented by F_{M1} and F_{M2}. The displacements of the input ends of springs due to these forces are shown with x_1 and x_2, respectively. We define:

$$x_c = \tfrac{1}{2}(x_1 + x_2) \tag{1}$$

$$x_d = \tfrac{1}{2}(x_1 - x_2) \tag{2}$$

By analogy to the action of muscles about a joint, x_c corresponds to co-activation while x_d corresponds to differential activation. By differential activation, the muscles are able to bias the pitch angle of the wing to a unique position, ψ_0. From Fig. 4, it can easily be seen that:

$$x_d = R\psi_0 \tag{3}$$

Any load on the wing – i.e., the aerodynamic force – will cause a further deflection from this equilibrium by an amount of Δ_ψ. The new angular position ψ determines the displacement of the output end of each spring. At any given time, this displacement is equal to:

$$R\psi = R\,(\psi_0 + \Delta_\psi) \tag{4}$$

where spring 1 moves to the left and spring 2 moves to the right. The deflection of each spring is the difference between the motions of its two ends. Using (1)-(4), it can be

shown that these deflections are as follow:

$$\delta_1 = x_c - R\Delta_\psi \tag{5}$$

$$\delta_2 = x_c + R\Delta_\psi \tag{6}$$

Depending on the amount of its deflection, each spring applies a force to the pulley, i.e. $F_i(\delta_i)$, $i=1,2$. The stiffness of each spring is also a function of its deflection: $\sigma_i(\delta_i)$. Note that stiffness is the derivative of force with respect to displacement:

$$\sigma_i(\delta_i) = \frac{d}{d\delta_i}F_i(\delta_i), \qquad i=1,2 \tag{7}$$

The forces developed in the stretched springs must then balance the externally applied torque τ_{ext}:

$$\tau_{ext} = R\big[F_2(\delta_2) - F_1(\delta_1)\big] \tag{8}$$

The effective joint stiffness k_{rot} is defined as the derivative of this torque with respect to the angular position ψ. By using the chain rule along with (5)-(8), we have:

$$k_{rot} = \frac{d}{d\psi}\tau_{ext} = R^2\big[\sigma_1(\delta_1) + \sigma_2(\delta_2)\big] \tag{9}$$

From (9), it can be seen that if individual springs are linear (constant stiffness σ_i), the effective joint stiffness is always a constant. Therefore, to model the joint with variable stiffness, nonlinear springs are required.

The diagram in Fig. 4 suggests that stiffness of the joint is primarily influenced by x_c. However, fast rotation of the wing may also affect k_{rot} [7]. Therefore, in reality k_{rot} slightly depends on the deflection of the joint from its equilibrium position, i.e. Δ_ψ. Here, in order to come up with a simple model for nonlinearity of the springs, we assume that k_{rot} is independent of Δ_ψ. Thus:

$$\frac{d}{d\Delta_\psi}k_{rot} = 0 = R^2\left[\frac{d}{d\Delta_\psi}\sigma_1(\delta_1) + \frac{d}{d\Delta_\psi}\sigma_2(\delta_2)\right] \tag{10}$$

which, from (5)-(6), will result in the following mathematical requirement:

$$\frac{d}{d\delta_1}\sigma_1(\delta_1) = \frac{d}{d\delta_2}\sigma_2(\delta_2) \tag{11}$$

whose general solution is given as:

$$\sigma_i(\delta_i) = A\delta_i + B_i, \qquad i=1,2 \tag{12}$$

where A and B are constant coefficients. Assuming that the joint is symmetric, i.e. the springs are identical, the subscript i on the constant B can be dropped. The force function for both springs will then have the following form:

$$F_i(\delta_i) = \tfrac{1}{2}A\delta_i^2 + B\delta_i + C, \qquad i=1,2 \tag{13}$$

in which, C is another constant coefficient. From (13),

quadratic springs are the type of nonlinearity that can satisfy (11). This type of spring has been previously used to predict the mechanical response of muscles during contraction with an error no more than 15% [8]. Therefore, when used in the setup of Fig. 4, such springs should provide a reasonable model of synchronous muscles' performance.

By replacing (5), (6) and (12) in (9), it can be shown that k_{rot} is now a pure function of co-activation:

$$k_{rot} = 2R^2 \ (Ax_c + B) \tag{14}$$

Similarly, using (3)-(6), (8) and (13)-(14), we can see that:

$$\tau_{ext} = k_{rot} \ (\psi - \psi_0) \tag{15}$$

Note that from (3), ψ_0 is proportional to x_d. Thus, the joint can be modeled as a torsional spring whose stiffness and set point are respectively controlled by co-activation and differential activation of the synchronous muscles.

III. AERODYNAMICS

Aerodynamics of insect flight, which corresponds to low Reynolds number (less than 3,000), has become a popular area of research over the past few decades, especially after [9]. In particular, scaled models of flapping wings [6], [10] have been very helpful in comprehending the involved unsteady-state aerodynamic mechanisms both qualitatively and quantitatively. Results obtained with the apparatus developed in [6], known as Robofly, have identified three main mechanisms: *delayed stall*, *rotational circulation*, and *wake capture*. Detailed descriptions of these mechanisms are available in [6], [11]-[12]. Here, we will briefly review the first-order models developed to estimate the aerodynamic forces produced by each mechanism. Using Blade Element Method (BEM) [9], [13]-[15], these models allow us to estimate the overall aerodynamic force for any given wing shape and stroke profile.

A. Mathematical Force Models

Reynolds number in insect flight is low enough to assume that air flow across the wing is quasi-stationary [11]-[14]. A quasi-steady-state aerodynamic model assumes that the force expressions derived for 2-D thin airfoils translating with constant angle of attack and constant velocity can be also used for time-varying 3-D flapping wings.

Essentially, delayed stall is the results of wing's translational motion [6]. Basic aerodynamic theory [16] shows that in steady-state conditions, the aerodynamic force per unit length on an airfoil due to its translational motion is given by:

$$f_N = \frac{\rho}{2} c C_N(\alpha_r) \ u_r^2 \tag{16}$$

$$f_{Tn} = \frac{\rho}{2} c C_T(\alpha_r) \ u_r^2 \tag{17}$$

where f_N and f_{Tn} are the normal and tangential components of the force. Note that these forces always oppose the stroke of the wing. Parameters ρ, c and α_r respectively represent the density of air, cord width of the airfoil and its angle of attack relative to air velocity u_r (Fig. 3.a).

C_N and C_T are dimensionless force coefficients which are generally time-dependent. However, experimental results in [6] suggest that a good quasi-steady-state empirical approximation for these coefficients due to delayed stall is given by:

$$C_N(\alpha_r) = 3.4 \sin \alpha_r \tag{18}$$

$$C_T(\alpha_r) = \begin{cases} 0.4 \cos^2(2\alpha_r), & 0 \le \alpha_r \le 45° \\ 0, & otherwise \end{cases} \tag{19}$$

The lift force due to rotational circulation of air around an airfoil has been modeled in [17]:

$$f_{N,rot} = \frac{\rho}{2} c^2 C_{rot} u_r \dot{\alpha}_r \tag{20}$$

where C_{rot} is the dimensionless rotational force coefficient. In flapping flight, this coefficient is also generally time-dependent. However, when using a constant value of $C_{rot} = \pi$ [12], quasi-steady-state modeling has provided satisfactory predictive capabilities [18]. Note that the derivative of α_r in (20) is in fact, an approximation of the wing's angular velocity. As a reminder, $f_{N,rot}$ is a pure pressure force that acts normal to the airfoil profile and in the opposite direction of wing's velocity.

Wake capture is a more complex mechanism. At the end of each half-stroke, the wing begins to change direction. However, the fluid behind the wing tends to maintain its velocity due to its inertia. Hence, the difference between velocities of fluid and wing results in production of a large force at the beginning of next half-stroke [6]. This phenomenon cannot be easily described by a quasi-steady-state model. However, it is observed to have an insignificant overall role when stroke profile is sinusoidal-like [11]. Since our simulations are based on this type of motion, the effect of wake capture is not considered in the rest of this paper.

B. Blade Element Method: Force Exerted on the Wing

In blade-element theory, a wing is divided into a set of cross-sectional strips, each of width dr, and located at a mean radius r from axis of wing stroke [15], as illustrated in Fig. 5. Each one of these strips is treated as an airfoil whose cord width is a function of r. The aerodynamic force for any airfoil can be then calculated using (16)-(20).

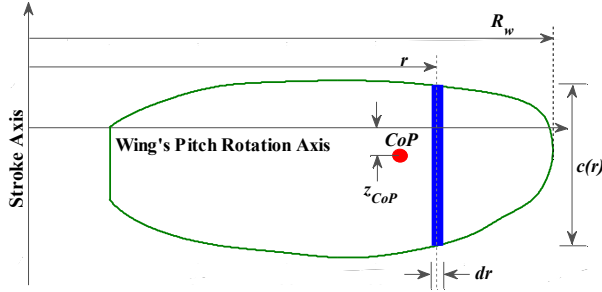The air velocity observed by an airfoil at radius r is given

Fig. 5. The wing shape used in all modeling/simulations and one of its blade elements. The span of the wing is represented by R_w.

by:

$$u_r = r\dot{\phi} \tag{21}$$

in which, ϕ is the stroke angle as defined in Fig 3.b. As mentioned earlier, we assume that stroke profile is sinusoidal:

$$\phi = \phi_0 \cos(\omega\, t) \tag{22}$$

where ϕ_0 and ω are the magnitude of the stroke and flapping frequency, respectively.

In our simulations, we consider the wing as a rigid, thin plate shaped as shown in Fig. 5. Replacing (21) in (16)-(17), (20) and integrating them over the span of this wing shape will result in the following expressions for total aerodynamic forces:

$$F_{N,trs} = 0.0442\rho\, C_N(\alpha_r)\, \dot{\phi}^2 R_W^4 \tag{23}$$

$$F_{Tn} = 0.0442\rho\, C_T(\alpha_r)\, \dot{\phi}^2 R_W^4 \tag{24}$$

$$F_{N,rot} = 0.0595\rho\, \dot{\alpha}_r\dot{\phi}\, R_W^4 \tag{25}$$

where R_W represents the span of the wing. F_{Tn} is the tangential force while $F_{N,trs}$ and $F_{N,rot}$ are the translational and rotational components of the normal force, F_N:

$$F_N = F_{N,trs} + F_{N,rot} \tag{26}$$

For the stroke profile in (22), the total aerodynamic force on the wing can be then estimated through (18)-(19) and (23)-(26). However, this estimation is still a function of α_r and its derivative.

From Section II, the balance between mechanical impedance of the joint and external load, i.e. the aerodynamic force, is what determines how the angle of attack should evolve. In the next section, we will further investigate this evolution as the potential underlying mechanism for force regulation in insect flight.

IV. FORCE CONTROL IN INSECT FLIGHT

In Section II, we argued that asynchronous muscles are the reason for the high wing beat rate in many insects.

Thus, they can be thought of as the main power source for production of aerodynamic force and hence, levitation. The structure of these muscles allows for changes in the magnitude of stroke and perhaps the frequency of flapping, both of which are parameters that influence the amount of generated aerodynamic force (Section III.B). However, the indirect connection of these muscles to the joint (Fig. 2) suggests that their contraction always affects both wings in the same way.

Maneuverability and flight control on the other hand, require that lift and thrust forces of each wing are individually adjusted. To change the lift and thrust components of the aerodynamic force produced by one wing, the insect needs to regulate the angle of attack of that wing. Direct attachment of one pair of synchronous muscles to each wing's joint makes them a convenient mechanism for this purpose. Evolution of angle of attack and the potential role of synchronous muscles in flight control are discussed next.

A. Evolution of Angle of Attack

In reality, aerodynamic force is distributed over the surface of the wing. However, it can equivalently be modeled as a force applied to a single point [12] called the center of pressure (CoP in Fig. 3 and Fig. 5). The location of this point, in general, depends on the wing's shape and can be estimated by calculation of aerodynamic force/torque pairs through BEM [15]. The distance of CoP from the wing's pitch rotation axis, i.e. z_{CoP}, determines the external load on the joint due to aerodynamic force F_N (Fig 3.a). Note that tangential force F_{Tn} does not influence the pitch rotation of the wing. For our choice of wing shape, estimation of z_{CoP} results in:

$$z_{CoP} = 0.0673\, R_W \tag{27}$$

The overall load tending to change the pitch angle of the wing is given by:

$$\tau_{ext} = z_{CoP}\, F_N - b_\psi\dot{\psi} - J_\psi\ddot{\psi} \tag{28}$$

where J_ψ and b_ψ are the moment of inertia and passive damping coefficient of the wing along its pitch rotation axis, respectively.

To maintain the balance, right hand sides of (15) and (28) must always remain equal. From Fig. 3.a, it can be seen that angle of attack and pitch angle of the wing are complementary angles, i.e. $\alpha_r = \pi/2 - \psi$. This allows us to rewrite (23)-(25) as functions of ψ and its derivative. Then the following ODE can be written using (15) and (28):

$$J_\psi\ddot{\psi} + b_\psi\dot{\psi} + k_{rot}\,(\psi - \psi_0) - z_{CoP}\, F_N(\psi,\dot{\psi}) = 0 \tag{29}$$

Using the aerodynamic force model of Section III, (29) can be numerically solved for a given stroke profile ϕ and
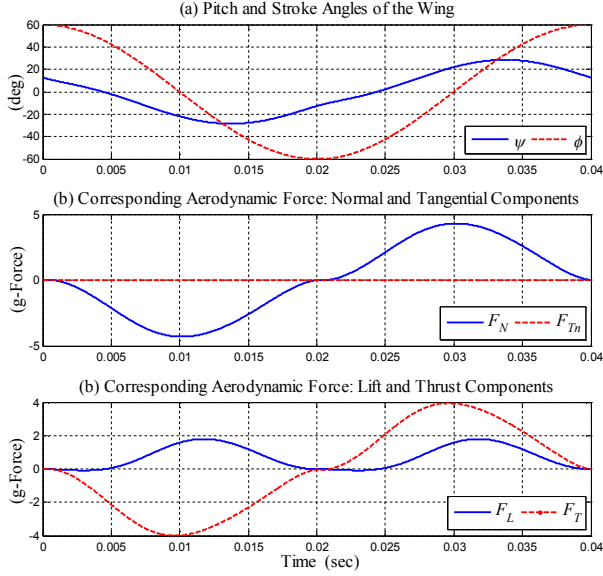
Fig. 6. (a) Simulated pitch and stroke angles of the wing for a large dragonfly. Stroke has a magnitude of 60° and a rate of 25 Hz. Impedance properties are set to $k_{rot} = 1.4 \times 10^{-3}$ N.m/rad and $\psi_0 = 0°$. The corresponding aerodynamic force is plotted both in (b) normal/tangential and (c) lift/thrust formats.

any desired set of wing joint impedance properties, i.e. k_{rot} and ψ_0. Once the waveform of ψ is found, aerodynamic forces F_N and F_{Tn} can be calculated for any given time. The lift and thrust components of the overall force, i.e. F_L and F_T, are also defined as illustrated in Fig. 3.a:

$$F_L = F_N \cos \alpha_r - F_{Tn} \sin \alpha_r \qquad (30)$$
$$F_T = -F_N \sin \alpha_r - F_{Tn} \cos \alpha_r \qquad (31)$$

Fig. 6.a. illustrates the solution to (29) for a single sinusoidal stroke cycle with $\phi_0 = 60°$ and $\omega = 50\pi$ rad/sec. These values are based on flight characteristics of a large dragonfly or a medium-sized hummingbird [1]. The values of other necessary physical parameters are listed in Table I. In this diagram, the case of no differential activation has been considered, i.e. $x_d = 0$ m. From (3), this means that $\psi_0 = 0°$. As for stiffness, we have chosen a value of $k_{rot} = 1.4 \times 10^{-3}$ N.m/rad which is soon shown to be the average-lift-optimizing value for the considered scale.

As Fig 6a suggests, during every half stroke, the wing smoothly rotates and adapts its angle of attack to the

TABLE I
PHYSICAL PARAMETERS USED IN SIMULATIONS OF SECTION IV

Symbol	Description	Value
ρ	air density at sea level	1.28 kg/m³
R_W	average span of each wing in a large dragonfly	8×10^{-2} m
J_ψ	moment of inertia of each wing (pitch rotation)	1.5×10^{-4} N.m.s²
b_ψ	passive damping coefficient of each wing (pitch rotation)	1×10^{-8} N.m.s
m_{body}	estimated mass of a two-winged MAV with similar dimensions	4×10^{-3} kg
g	standard gravity at sea level	9.81 m/s²

upcoming air flow. Through this rotation, the balance between aerodynamic force and impedance of the joint is maintained.

The normal/tangential and lift/thrust components of the corresponding aerodynamic force are illustrated in Fig. 6.b and Fig. 6.c, respectively. Every force curve has been normalized by the estimated weight of a same-sized MAV (Table I). Fig. 6.c reveals that for $\psi_0 = 0°$, the profile of lift force is even-symmetric and has an average value of 0.7252 g-Force per wing. Note that this value is about 45% larger than what is required to levitate a two-winged MAV of target size and weight. Production of such large forces is in agreement with the highly agile movements that are often demonstrated by insects/hummingbirds.

On the other hand, the thrust profile in Fig. 6.c is odd-symmetric; it has an average value of 9.312×10^{-7} g-Force per wing. This practically zero average thrust force verifies that insects such as flies are able to hover, another flight capability that is seldom observed outside of the insect world.

A change in contraction level of synchronous muscles can reshape the profile of ψ and lift/thrust forces. In the remainder of this section, we will investigate how insects might use these changes to adjust the aerodynamic forces, and thereby, achieve flight control.

B. Force Control through Impedance Tuning

Stiffness of the joint is a limiting factor for pitch rotation of the wing. A very stiff joint tends to move less and thus, does not allow the wing to reach low angles of attack (Fig. 7.a). This leads to reduction of the lift force (Fig. 7.b).

Although changing k_{rot} results in different magnitudes of thrust force in Fig. 7.c, it is observed that as long as $\psi_0 = 0°$,
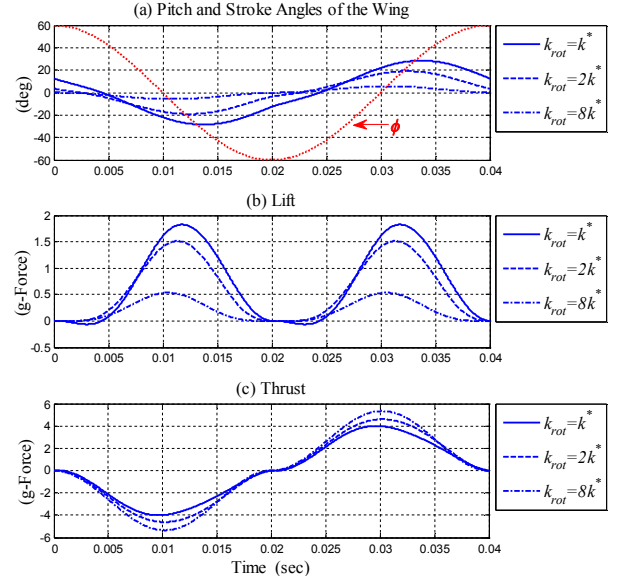

Fig. 7. (a) Simulated pitch and stroke angles of the wing for a large dragonfly. Stroke has a magnitude of 60° and a rate of 25 Hz. Here, $\psi_0 = 0°$ while k_{rot} is set to different multiples of $k^* = 1.4 \times 10^{-3}$ N.m/rad. The corresponding (b) lift and (c) thrust forces are also plotted for comparison.
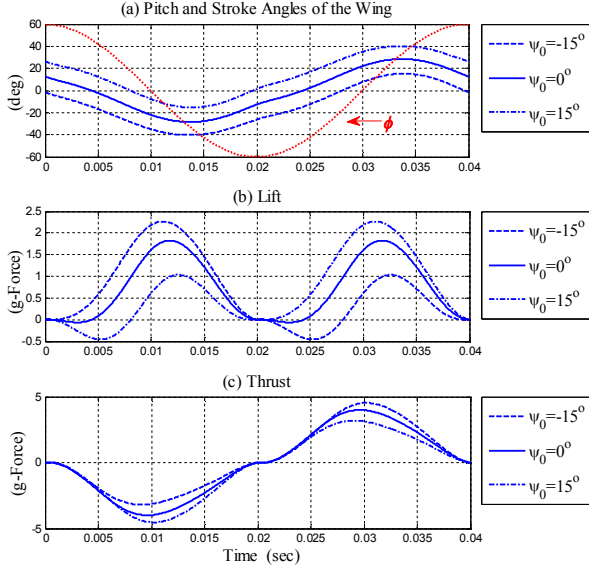
Fig. 8. (a) Simulated pitch and stroke angles of the wing for a large dragonfly. Stroke has a magnitude of 60° and a rate of 25 Hz. Here, k_{rot} = 1.4×10^{-3} N.m/rad while different values of ψ_0 are examined. The corresponding (b) lift and (c) thrust forces are also plotted for comparison.

Fig. 9. (a) Average lift and (b) average thrust forces vs. set point and stiffness of the wing's joint.

the profile of this force remains odd-symmetric. To produce a net thrust force for forward/backward motion or steering, the insect needs to somehow disturb this symmetry. Fig. 8 shows how an asymmetric thrust profile can be achieved through changing the set point of the joint.

Impedance set point, i.e. ψ_0, acts as a bias added to the pitch angle of the wing. The resulting shift in the waveform of ψ (Fig. 8.a) creates asymmetries in both lift (Fig. 8.a) and thrust profiles (Fig. 8.c). For $\psi_0 = \pm15°$, the average lift force in Fig. 8.b is equal to 0.6366 g-Force per wing. Note that this value is still about 27.3% larger than the required force for levitation of a same-sized two-winged MAV. As for thrust profiles in Fig. 8.c, the induced asymmetries by negative and positive set points create a net thrust force of 0.3098 and -0.3098 g-Force per wing, respectively.

Fig. 9 illustrates how net lift and thrust forces are influenced by simultaneous variations in stiffness and set point. From Fig. 9.a, maximum average lift is achievable when k_{rot} = 1.4×10^{-3} N.m/rad and ψ_0 = 0°. To provide a better view, cross-sections of the surfaces in Fig. 9 at these values are plotted in Fig. 10.

Fig. 10.a suggests that through regulation of k_{rot}, insects are able to manipulate their lift force and thus ascend or descend. Interestingly, as long as ψ_0 is sufficiently small, changes in k_{rot} have little effect on the net thrust force. From Fig. 10.b, it is observed that changing ψ_0 between ±40° can produce significant amounts of net thrust force. These values are large enough to support agile horizontal maneuvers such as steering and forward/backward motion. In addition to production of considerable net thrust, when ψ_0 is between ±15°, the observed attenuation in net lift is no larger than 13%. Therefore, as long as set point variations
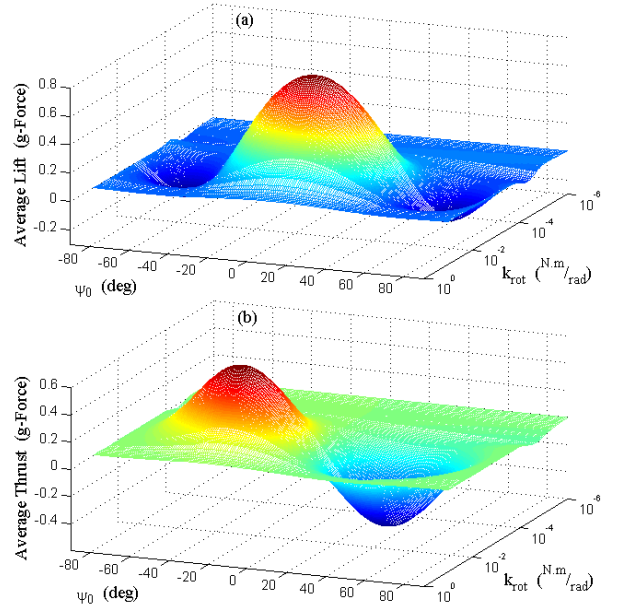
are limited, net values of lift and thrust forces can be controlled almost independently. This is a feature that significantly improves maneuverability and flight control.

Finally, we emphasize that from (3) and (14), set point and stiffness of the wing's joint are respectively adjusted by differential and co-activation of synchronous muscles. Since both of these dependencies are linear, it is easy to see that the pair (x_d, x_c) affects net lift and thrust forces in the same way as (ψ_0, k_{rot}).

V. DYNAMIC MODEL OF THE MAV

Performance of the proposed force regulation approach is evaluated through a set of simulated flight experiments with a modeled two-winged MAV. The free-body diagram of this
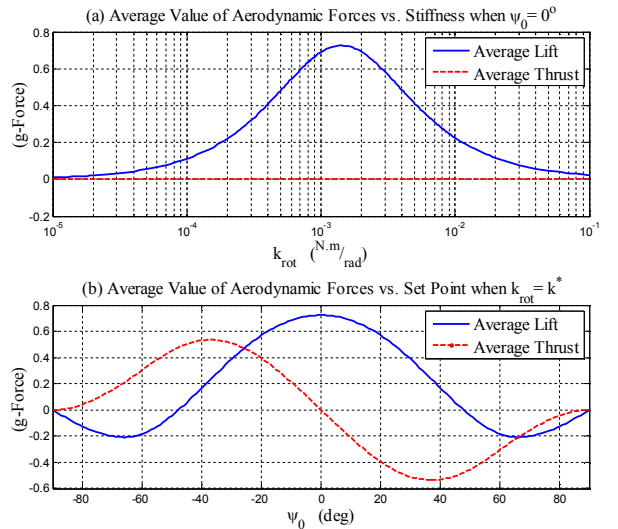

Fig. 10. (a) Average lift and thrust forces vs. stiffness of the joint when $\psi_0 = 0°$. The maximum value of lift is achieved for $k_{rot} = k^* = 1.4×10^{-3}$ N.m/rad. (b) Average lift and thrust forces vs. set point of the joint when k_{rot} is kept at k^*.
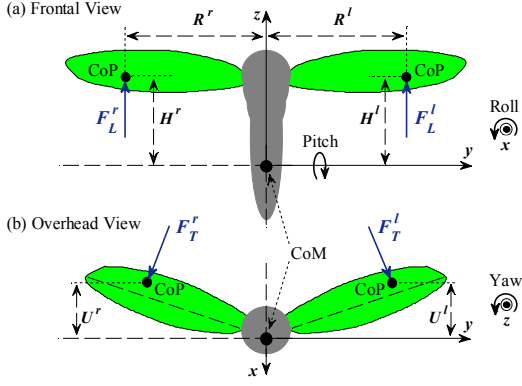
Fig. 11. Free-body diagram of a flapping-wing MAV: (a) frontal and (b) overhead views. *H*, *R* and *U* are the distance components of center of pressure (CoP) of each wing from center of mass (CoM) of the whole system.

flapping-wing MAV is shown in Fig. 11. This body structure is based on the vehicle in [19]. The shape of each wing is the same as Fig. 5 and other characteristics of the wings are assumed to be as reported in Table I.

The six-degree-of-freedom dynamic model of the vehicle [12] is developed by applying Newton's equations of motion in the body frame of Fig. 11:

$$m_{body} \ (\dot{\vec{v}} + \vec{\omega} \times \vec{v}) = \Sigma \vec{F} \tag{32}$$

$$= \vec{F}^l + \vec{F}^r - m_{body} \vec{G} - b_v |\vec{v}| \vec{v}$$

$$J_{body} \dot{\vec{\omega}} + \vec{\omega} \times J_{body} \vec{\omega} = \Sigma \vec{\tau} \tag{33}$$

$$= \vec{D}^l \times \vec{F}^l + \vec{D}^r \times \vec{F}^r - b_\omega \vec{\omega}$$

where:

$$\vec{F}^l = \begin{bmatrix} F_T^l \cos \phi^l \\ F_T^l \sin \phi^l \\ F_L^l \end{bmatrix}, \quad \vec{F}^r = \begin{bmatrix} F_T^r \cos \phi^r \\ -F_T^r \sin \phi^r \\ F_L^r \end{bmatrix} \tag{34}$$

and:

$$\vec{D}^l = \begin{bmatrix} U^l \\ R^l \\ H^l \end{bmatrix}, \quad \vec{D}^r = \begin{bmatrix} U^r \\ -R^r \\ H^r \end{bmatrix} \tag{35}$$

The vector $\vec{G}$ expresses gravity in the body coordinate frame. Euler angles in the Tait-Bryan ZXY convention are used to keep track of the orientation of the body with respect to the reference coordinates. Translational and angular velocities of the MAV are represented by vectors $\vec{v}$ and $\vec{\omega}$, respectively. *H*, *R* and *U* are the distance components of center of pressure of each wing from the overall center of mass (CoM), as shown in Fig. 11. The parameter b_v is the coefficient of viscous friction and the term with b_ω is used to model the effect of passive rotational damping, as discussed in [20]. The values of these parameters are listed in Table

II.

Total body mass − m_{body} − is assumed to be 4×10^{-3} kg for a vehicle of desired scale (Table I). The body shape in Fig. 11 is chosen since its corresponding inertia matrix relative to the center of mass (CoM), i.e. J_{body}, has insignificant nondiagonal terms and thus, can be approximated by:

$$J_{body} = \begin{bmatrix} 30 & 0 & 0 \\ 0 & 3 & 0 \\ 0 & 0 & 3 \end{bmatrix} \times 10^{-5} \text{ N.m.s}^2 \tag{36}$$

VI. CONTROLLER

Fig. 12 illustrates the block diagram of the employed control module in simulations of Section VII. A total of three sub-controllers are responsible for stabilization of pitch angle and regulation of lift and thrust forces, thus controlling vertical/horizontal maneuvers. In simulations, the controller is implemented as a discrete-time system with a fixed time-step of 0.01 seconds, i.e. per each stroke cycle, 4 sets of control commands are sent to the simulated MAV. The structure of each sub-controller is briefly discussed next.

A. Pitch Controller

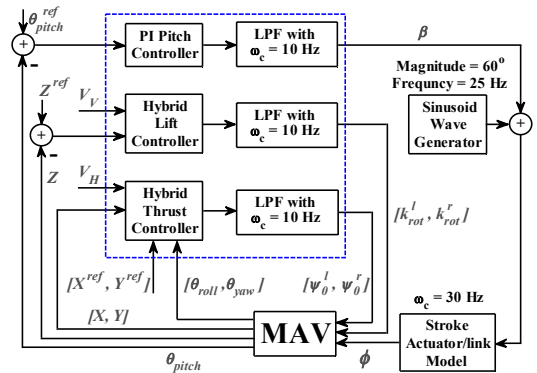For a sinusoidal stroke profile with no bias, the average

Fig. 12. Block diagram of the control module and its interaction with the simulated MAV. In each stroke cycle, the sinusoid wave generator creates a reference stroke waveform with a fixed magnitude of 60° at 25 Hz which will be then biased with β. Crossover frequency of each filter/actuator is represented by ω_c.

position of center of lift (CoL) for the flapping-wing MAV of Fig. 11 is not directly above its CoM. In a real MAV, similar situations can occur when the position of CoM changes due to modifications or carrying a payload. In such scenarios, the pitch torque can quickly destabilize the vehicle and causes it to crash by over-pitching.

To stabilize the pitch angle of the vehicle, i.e. θ_{pitch}, we employed a PI controller whose output β is used to bias the stroke angle of the wings in order to keep the average position of CoL above CoM. Note that at all times, both wings have the same stroke profile of the form:

$$\phi = \phi_0 \cos(\omega\, t) + \beta \qquad (37)$$

The reference pitch angle in Fig. 12, i.e. $\theta_{pitch}{}^{ref}$, may vary depending on the required maneuver, but in our simulations, we never had to use a value larger than 4° in magnitude. Note that β is saturated at ±15° to ensure that the stroke angles remain between -75° and 75°. It is also low-pass filtered in order to simulate a smooth transition in the amount of stroke bias (Fig. 12).

B. Lift Controller

The relationship between k_{rot} and average production of lift force is employed in a hybrid controller to regulate the altitude of the vehicle. If the vehicle is supposed to change its altitude Z, a proportional controller is responsible to stabilize the average vertical velocity at a reference value of $V_V = 1$ m/s. This reference value is decreased when the vehicle is within 10 cm of its desired altitude. Upon satisfaction of the necessary conditions ($|\Delta Z| < 0.01$ m and $|\dot{Z}| < 0.1$ m/s), command is switched to a PID controller that stabilizes the vehicle's vertical position at the target altitude.

From Fig. 10.a, the nominal value of k_{rot} is chosen equal to 3.7×10^{-3} N.m/rad to ensure sufficient lift production for levitation. To regulate the production of lift force, k_{rot} is only allowed to change within the interval $[1.4 \times 10^{-3}, 1.11 \times 10^{-2}]$ N.m/rad. Finally, to avoid sudden changes in the value of stiffness and to simulate its smooth transition as a mechanical parameter, the outputs of the lift controller are low-pass filtered prior to being applied to the simulated MAV (Fig. 12).

C. Thrust Controller

Another hybrid controller is responsible for thrust control by adjusting the set points of the wings' joints. Initially, based on current orientation and position of the MAV along with the position of the target, the deviation angle is calculated. If this angle is between 2° and 178°, ψ_0 is calculated proportional the deviation angle from the target. This value determines the magnitude of set point angles for both wings but the signs should be opposite and are determined according to the required direction of steering (Fig. 10.b).

Once the deviation angle is within the acceptable range, another sub-controller will be activated to govern horizontal motion and position stabilization. This part is structurally identical to the lift controller and uses the same values for reference horizontal velocity – $V_H = 1$ m/s – and internal switching conditions. However, the output of the controller is now used to adjust the set points of the wings. Note that in this case, the net thrusts of both wings must be in the same direction. Thus, the set points of the wings' joints should have the same sign (Fig. 10.b).

The activation of thrust controller is accompanied with production of yaw and roll torques. While steering relies on yaw torques, roll torques can destabilize the roll angle of the vehicle, i.e. θ_{roll}, and cause undesired lateral motion. To avoid this, we can create a small imbalance between the average lift forces of the wings through further manipulation of their joints' set points. From Fig. 10.b, a slight attenuation in the magnitude of a non-zero set point will slightly increase the average production of lift force by the corresponding wing. By doing so for the side that vehicle has rolled to, the extra lift force on that side will result in a roll torque that tends to decrease the magnitude of θ_{roll} and keep it close to 0°. For this purpose, the attenuation factor γ is calculated as follows:

$$\gamma = \max(0,\ 1 - \eta|\theta_{roll}|) \qquad (38)$$

where $\eta = 100$ is a constant gain.

The value of ψ_0 is nominally 0° and the thrust controller can change it within the interval [-15°, 15°]. This range is chosen to avoid significant intervention with lift production (Fig. 10.b). In addition, to prevent sudden changes in the values of joints' set points and to simulate their smooth transition as mechanical parameters, the outputs of the thrust controller are fed to a low-pass filter prior to being applied to the simulated MAV (Fig. 12).

VII. Flight Simulations

To evaluate the performance of proposed force/motion control approach, sample results of simulated flight experiments using the MAV model and controller from Sections V and VI will be presented and discussed next. The gains and time constants of the controller are set to reasonable values through a group of preliminary tuning experiments. The tuned sub-controllers are listed in Table III.

TABLE III
TUNED SUB-CONTROLLERS

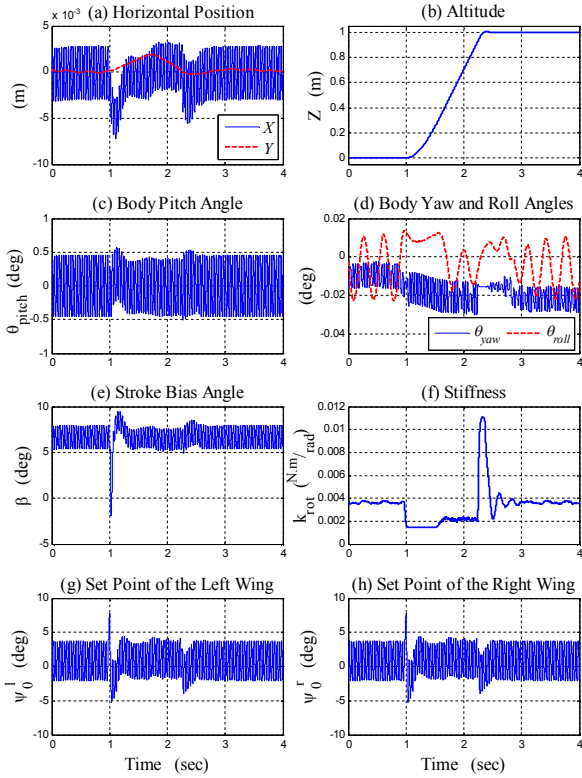| Transfer Function	Description
10+0.1/s	PI pitch controller
25	proportional vertical velocity controller
100+1/s+5s	PID vertical position controller
75	proportional steering controller
25	proportional horizontal velocity controller
500+1/s+100s	PID horizontal position controller

Fig. 13. A simulated takeoff/hovering experiment: (a) *X* and *Y* components of horizontal position, (b) altitude *Z*, (c) body pitch angle, (d) body yaw and roll angles, (e) stroke bias angle, (f) stiffness of the wings' joints, (g) set point angle of the left and (h) right wings.

Fig. 14. A simulated pitch tracking experiment: (a) *X* and *Y* components of horizontal position, (b) altitude *Z*, (c) body pitch angle, (d) body yaw and roll angles, (e) stroke bias angle, (f) stiffness of the wings' joints, (g) set point angle of the left and (h) right wings.

A. Takeoff and Hovering

The simulated position and orientation of the MAV during a takeoff/hovering experiment are plotted in Fig. 13. The vehicle is initially in hovering mode and at t=1 sec, it starts to increase its altitude by 1 m. After reaching the target altitude, hovering mode is resumed.

Fig. 13 demonstrates a smooth and agile motion with negligible orientation/position error. Note that during takeoff, the vehicle tends to move in the horizontal plane (Fig. 13.a). This is due to the fact that changing k_{rot} affects the instantaneous value of thrust forces as well as lift (Fig. 7). However, the thrust controller is able to quickly restabilize the MAV by applying small changes in the set point angles of both wings (Fig. 13.g and h).

B. Pitch Tracking

Considerable changes in the pitch angle of the body are often required when an aerial vehicle is performing an agile maneuver. Therefore, it is very important that the controller can keep up with such changes while maintaining the stability of the vehicle. To investigate the performance of our approach under these circumstances, we have examined the case of a hovering MAV which is supposed to adapt the pitch angle of its body to various sequences of rapidly changing reference values. The simulated results of one such trial are plotted in Fig. 14.

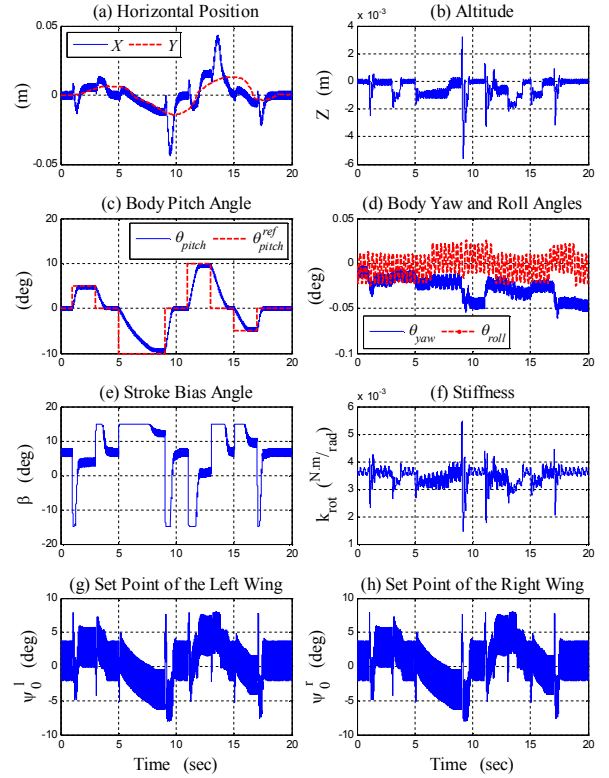The reference sequence is shown in Fig. 14.c along with

the corresponding body pitch angle of the MAV. As the vehicle pitches, the direction of average aerodynamic force in the reference coordinates changes. Therefore, the MAV tends to move in both horizontal and vertical directions (Fig. 14.a and b). However, by readjusting the impedance properties of the wings' joints, lift and thrust controllers manage to keep the vehicle close to its initial position without risking destabilization.

C. Three-dimensional Target Seeking

Reaching a specified target position, i.e. (X^{ref}, Y^{ref}, Z^{ref}), generally requires a combination of both steering and forward/backward motion along with altitude regulation. Thus, by simulating a three-dimensional motion, we can examine the simultaneous performance of both force controllers during movement. At the same time, we will be able to investigate whether or not our thrust control method interferes with the performance of lift controller.

Fig. 15 illustrates the simulated position and orientation of the MAV during one such experiment. Up to t=1 sec, the MAV is hovering at the origin while facing along the *X* axis. At this time, a new target is specified at (1 m, 1 m, 1 m). It takes 1.4 sec for the MAV to completely reorient towards the target (t = 2.4 sec in Fig. 15.d). Desired altitude is reached and stabilized within the next second (t=3.4 sec in Fig. 15.b). The maneuver is completed at t=4 sec when the vehicle reaches the target (Fig. 15.a). The vehicle is then
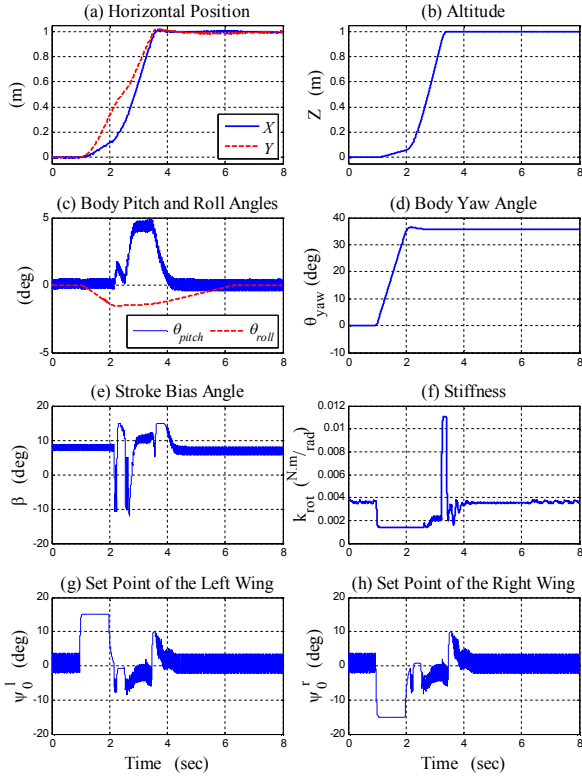
Fig. 15. A simulated three-dimensional target seeking experiment: (a) X and Y components of horizontal position, (b) altitude Z, (c) body pitch and roll angles, (d) body yaw angle, (e) stroke bias angle, (f) stiffness of the wings' joints, (g) set point angle of the left and (h) right wings.

Fig. 16. A simulated perturbation recovery experiment: (a) X and Y components of horizontal position, (b) altitude Z, (c) body pitch and roll angles, (d) body yaw angle, (e) stroke bias angle, (f) stiffness of the wings' joints, (g) set point angle of the left and (h) right wings.

quickly stabilized at the new location and resumes hovering. Overall, the simulated MAV demonstrates a smooth and agile motion. Note that during steering phase, the magnitude of body roll angle begins to increase. However, through the proposed countermeasure in Section VI.C, thrust controller is able to stabilize this angle and eventually bring it back to 0° (Fig. 15.c).

Both experiments of Fig. 13 and Fig. 15 require that MAV increases its altitude by 1 m. Comparing Fig. 13.b with Fig. 15.b reveals little difference in the way altitude changes. Fig. 13.f and 15.f also indicate small differences in the transition of stiffness. This proves that in the chosen operating ranges for mechanical impedance properties, thrust controller does not significantly interfere with the operation of lift controller.

D. Perturbation Recovery

The ability of the proposed force/motion control approach in handling perturbations and restabilization of the vehicle after an impact is another important performance measure that should be investigated. Various scenarios of this type have been simulated and the controller was always able to restore the balance of the MAV and resume its interrupted action within a very short amount of time.

The example in Fig. 16 illustrates one such trial. The vehicle is initially in hovering mode until at t=1 sec, it is briefly ($\Delta t = 7 \times 10^{-3}$ sec) exposed to a large external force –
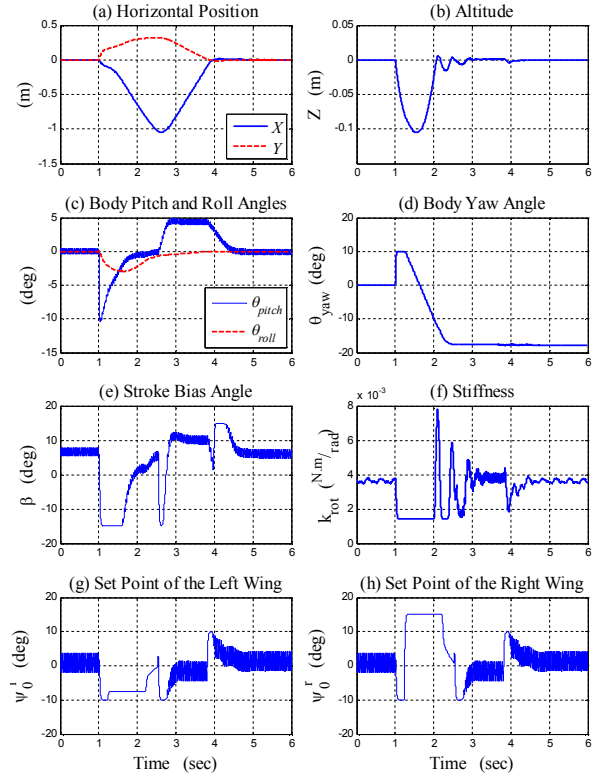
modeled as additional force and torque terms in (32) and (33) – from the right-front direction. By providing an initial velocity, the impact forces the MAV to move away from its hovering position (Fig. 16.a and Fig. 16.b). Furthermore, the torque produced by this force with respect to the CoM of the vehicle results in almost instantaneous jumps in pitch, roll and yaw angles of the vehicle (Fig. 16.c and Fig. 16.d).

After the impact, the vehicle has to resume hovering at its initial position. By t=2 sec, the pitch controller stabilizes θ_{pitch} (Fig. 16.c) through appropriate biasing of the stroke angles (Fig. 16.e). In the same period, the lift controller is able to bring the vehicle close to its initial altitude and stabilizes it within the next second (Fig. 16.b). Meanwhile, the thrust controller simultaneously reduces the roll angle (Fig. 16.c), reorients the vehicle towards the origin (Fig. 16.d) and decreases the induced horizontal velocity due to impact (Fig. 16.a). Steering is completed at t = 2.5 sec. However, while reducing the horizontal velocity, the vehicle considerably moves in the horizontal plane. Therefore, another 1.5 seconds is required until the MAV reaches its target and resumes hovering at t = 4 sec. Overall, the proposed control approach demonstrates a relatively fast response during all perturbation recovery experiments.

VIII. CONCLUSION

The combination of a simple muscle model and a quasi-

steady-state aerodynamic model makes it possible to estimate how angle of attack and aerodynamic forces of insect wings evolve as a sinusoidal stroke cycle is executed. The results of these simulations suggest that lift and thrust forces could be controlled through regulating the stiffness (co-activation of synchronous muscles) and set point (differential activation of synchronous muscles) of the wing's joint. Hence, synchronous muscles may play a key role in flight control capabilities of insects.

This potential mechanism of flight control in insects has inspired us to develop a similar approach for force/motion control in insect-like MAVs such as [19]. We refer to this method as "*Tunable Impedance*" (TI) technique. As of yet, this method has been only used to control simulated MAVs during various flight maneuvers. Simulations for one such vehicle – the size of a large dragonfly – were presented in Section VII. The results of experiments with a simulated fly-scale MAV using a preliminary version of this control approach are also available in [21]. In all experiments, the controller has demonstrated an exceptional performance that results in a high degree of maneuverability and agile motions.

One advantage of force control using TI technique is that it does not need to change the stroke profiles of the wings in order to generate lift/thrust or steering torques. Therefore, both wings have the same stroke profile at all times and can be driven with a single actuator in a real MAV. In contrast, ad hoc solutions such as "*Split Cycle*" (SC) method [22] assume that wings can have different stroke profiles and use the difference between corresponding forces to produce steering torques. This means that each wing must have its own stroke actuator. At the investigated scale in this paper, these actuators are usually dc motors that impose a considerable weight challenge in the design stage. Furthermore, solutions such as SC need to change the shape of stroke profile in order to regulate aerodynamic forces. For example, SC requires downstroke to be faster than upstroke during a forward thrust maneuver. Operating at higher frequencies increases the power consumption of stroke actuators which is another design problem due to limited weight for onboard batteries.

Implementation of the TI method on a real MAV calls for development of variable impedance actuators that meet certain shape/weight criteria. The diagram in Fig. 4 serves as a basic design scheme for such actuators; the tendons developed in [23] are a suitable replacement for quadratic springs. However, more complex and efficient designs are available for impedance alteration [24]-[26]. It is worth noting that in a MAV, impedance actuators have to deal with small loads and thus, can be piezoelectric-based or developed through MEMS technology. This will significantly reduce their weight and power requirements and greatly benefits the overall design problem.

To investigate the performance of TI technique in a real system, we are currently implementing it on a scaled bench-top flapping-wing tester. Our goal is to eventually use this method on a 3-inch-wingspan flapping-wing MAV.

REFERENCES

[1] R. Dudley, *The Biomechanics of Insect Flight: Form, Function, Evolution*. Princeton University Press, 2000.

[2] "Insect Wings," Internet: www.amentsoc.org/insects/fact-files/wings.html, 1997 [September 15, 2011].

[3] Z. Jane Wang, "Vortex shedding and frequency selection in flapping flight", *Journal of Fluid Mechanics,* 410, pp. 323-341, 2000.

[4] R. K. Josephson, "Chapter 3: Comparative Physiology of Insect Flight Muscle," in Nature's Versatile Engine: Insect Flight Muscle Inside and Out. (Vigoreaux and Josephson, ed.) pp. 34-43, Springer US, 2006.

[5] T. A. McMahon, *Muscles, Reflexes, and Locomotion*. Princeton University Press, 1984.

[6] M. H. Dickinson, F. Lehmann, and S. P. Sane, "Wing rotation and the aerodynamic basis of insect flight," *Science*, 284 (5422), pp. 1954-1960, 1999.

[7] R. Shadmehr, and S. P. Wise, *The Computational Neurobiology of Reaching and Pointing: A Foundation for Motor Learning*. The MIT Press, 2005.

[8] A. B. Schultz, J. A. Faulkner, and V. A. Kadhiresan, "A simple hill element-nonlinear spring model of muscle contraction biomechanics," *Journal of Applied Physiology*, 70 (2), pp. 803-812, 1991.

[9] C. P. Ellington, "The aerodynamic of hovering insect flight I. the quasi-steady analysis," *Philosophical Transactions of the Royal Society of London*, 305 (1122), pp. 1-15, 1984.

[10] A. Willmott, C. Ellington, C. van den Berg, and A. Thomas, "Flow visualisation and unsteady aerodynamics in the flight of the hawkmoth *Manduca sexta*," *Philosophical Transactions of the Royal Society of London*, B Biological Sciences, 352, pp. 303-316, 1997.

[11] S. Sane, "The aerodynamics of insect flight," *Journal of Experimental Biology*, 206, pp. 4191-4208, 2003.

[12] X. Deng, L. Schenato, W. C. Wu, and S. S. Sastry, "Flapping flight for biomimetic robotic insects: part I–system modeling," *IEEE Transactions on Robotics*, 22 (4), pp. 776–788, 2006.

[13] S. P. Sane, and M. H. Dickinson, "The control of flight by a flapping wing: lift and drag production," *Journal of Experimental Biology*, 204, pp. 2607-2626, 2001.

[14] W. B. Dickson, and M. H. Dickinson, "The effect of advance ratio on the aerodynamics of revolving wings," *Journal of Experimental Biology*, 207, pp. 4269-4281, 2004.

[15] K. Byl, "A passive dynamic approach for flapping-wing micro-aerial vehicle control," 2010 ASME Dynamic Systems and Control Conf., Cambridge, MA, USA, September 13-15, 2010.

[16] A. Kuethe, and C. Chow, *Foundations of Aerodynamics*, New York: Wiley, 1986.

[17] Y. Fung, *An Introduction to the Theory of Aeroelasticity*, New York: Dover, 1969.

[18] S. Sane, and M. Dickinson, "The aerodynamic effects of wing rotation and a revised quasi-steady model of flapping flight," *Journal of Experimental Biology*, 205, pp. 1087-1096, 2002.

[19] R. J. Wood, "The first takeoff of a biologically inspired at-scale robotic insect," *IEEE Transactions on Robotics*, 24, pp. 341–347, 2008.

[20] T. L. Hedrick, B. Cheng, and X. Deng, "Wingbeat time and the scaling of passive rotational damping in flapping flight," Science, 324, 2009.

[21] H. Mahjoubi, and K. Byl, "Analysis of a tunable impedance method for practical control of insect-inspired flapping-wing MAVs," 2011 IEEE Conference on Decision and Control and European Control Conference (CDC-ECC), Orlando, FL, USA, December 12-15, 2011.

[22] D. B. Doman, and M. W. Oppenheimer, "Dynamics and control of a minimally actuated biomimetic vehicle: part I. aerodynamic model," 2009 AIAA Guidance, Navigation, and Control Conf., San Francisco, CA, USA, August 10-13, 2009.

[23] T. Miura, T. Shirai, and T. Tomioka, "Proposal of joint stiffness adjustment mechanism SAT," JSME Conference on Robotics and Mechatronics '02, pp. 29, 2002. (in Japanese)

[24] G. Tonietti, R. Schiavi, and A. Bicchi, "Design and control of a variable

stiffness actuator for safe and fast physical human/robot interaction," 2005 IEEE International Conference on Robotics and Automation (ICRA), Barcelona, Spain, April 2005.

[25] R. Schiavi, G. Grioli, S. Sen, and A. Bicchi, "VSA-II: a novel prototype of variable stiffness actuator for safe and performing robots interacting with humans," 2008 IEEE International Conference on Robotics and Automation (ICRA), Pasadena, CA, USA, May 19-23, 2008.

[26] J. Choi, S. Hong, W. Lee, S. Kang, and M. Kim, "A robot joint with variable stiffness using leaf springs," *IEEE Transactions on Robotics*, 27 (2), pp. 229-238, April 2011.